


Real-time monitoring of reaction stereochemistry through single-molecule observations of chirality-induced spin selectivity

Received: 25 March 2022

Accepted: 20 April 2023

Published online: 15 May 2023

 Check for updates

Chen Yang^{1,6}, Yanwei Li^{2,3,6}, Shuyao Zhou¹, Yilin Guo¹, Chuancheng Jia⁴, Zhirong Liu¹, Kendall N. Houk³✉, Yonatan Dubi⁵✉ & Xuefeng Guo^{1,4}✉

Stereochemistry has an essential role in organic synthesis, biological catalysis and physical processes. In situ chirality identification and asymmetric synthesis are non-trivial tasks, especially for single-molecule systems. However, going beyond the chiral characterization of a large number of molecules (which inevitably leads to ensemble averaging) is crucial for elucidating the different properties induced by the chiral nature of the molecules. Here we report direct monitoring of chirality variations during a Michael addition followed by proton transfer and keto–enol tautomerism in a single molecule. Taking advantage of the chirality-induced spin selectivity effect, continuous current measurements through a single-molecule junction revealed in situ chirality variations during the reaction. Chirality identification at a high sensitivity level provides a promising tool for the study of symmetry-breaking reactions and sheds light on the origin of the chirality-induced spin selectivity effect itself.

Molecular chirality is well known for its key role in various chemical¹, physical² and especially life processes³. The sensitive detection^{4,5} of the chirality of (bio)molecules is thus of great interest to the field of drug development because of its importance in molecular recognition and function^{6–10}. Furthermore, such sensitive detection can lead to the recognition of asymmetric catalytic products, intermediates and even transition states, thus enhancing our understanding of stereoselective and chiral symmetry-breaking reactions.

Molecular chirality can be detected sensitively via polarized light or spin current, with an important example of spin current being the

chirality-induced spin selectivity (CISS) effect^{11–16}, whereby enantiomers provide different electrostatic potential barriers for the same spin carriers. Therefore, when electrons move through a chiral molecule, their transport is spin dependent: the preferred spin orientation is determined by the interplay between the chirality of the molecule and the direction of carrier motion. The CISS effect is expected to be applied to memristors¹⁷, non-dissipative transmission¹⁸, chirality detection⁸ and more^{12,18,19}. Although various theoretical models of CISS have been put forward^{16,19–23}, in practice, chiral molecules show several orders of magnitude more spin filtering than would theoretically be

¹Beijing National Laboratory for Molecular Sciences, National Biomedical Imaging Center, College of Chemistry and Molecular Engineering, Peking University, Beijing, People's Republic of China. ²Environment Research Institute, Shandong University, Qingdao, People's Republic of China. ³Department of Chemistry and Biochemistry, University of California, Los Angeles, Los Angeles, CA, USA. ⁴Center of Single-Molecule Sciences, Institute of Modern Optics, Frontiers Science Center for New Organic Matter, College of Electronic Information and Optical Engineering, Nankai University, Tianjin, People's Republic of China. ⁵Department of Chemistry, Ben-Gurion University of the Negev, Be'er-Sheva, Israel. ⁶These authors contributed equally: Chen Yang, Yanwei Li. ✉e-mail: houk@chem.ucla.edu; jdubi@bgu.ac.il; guoxf@pku.edu.cn

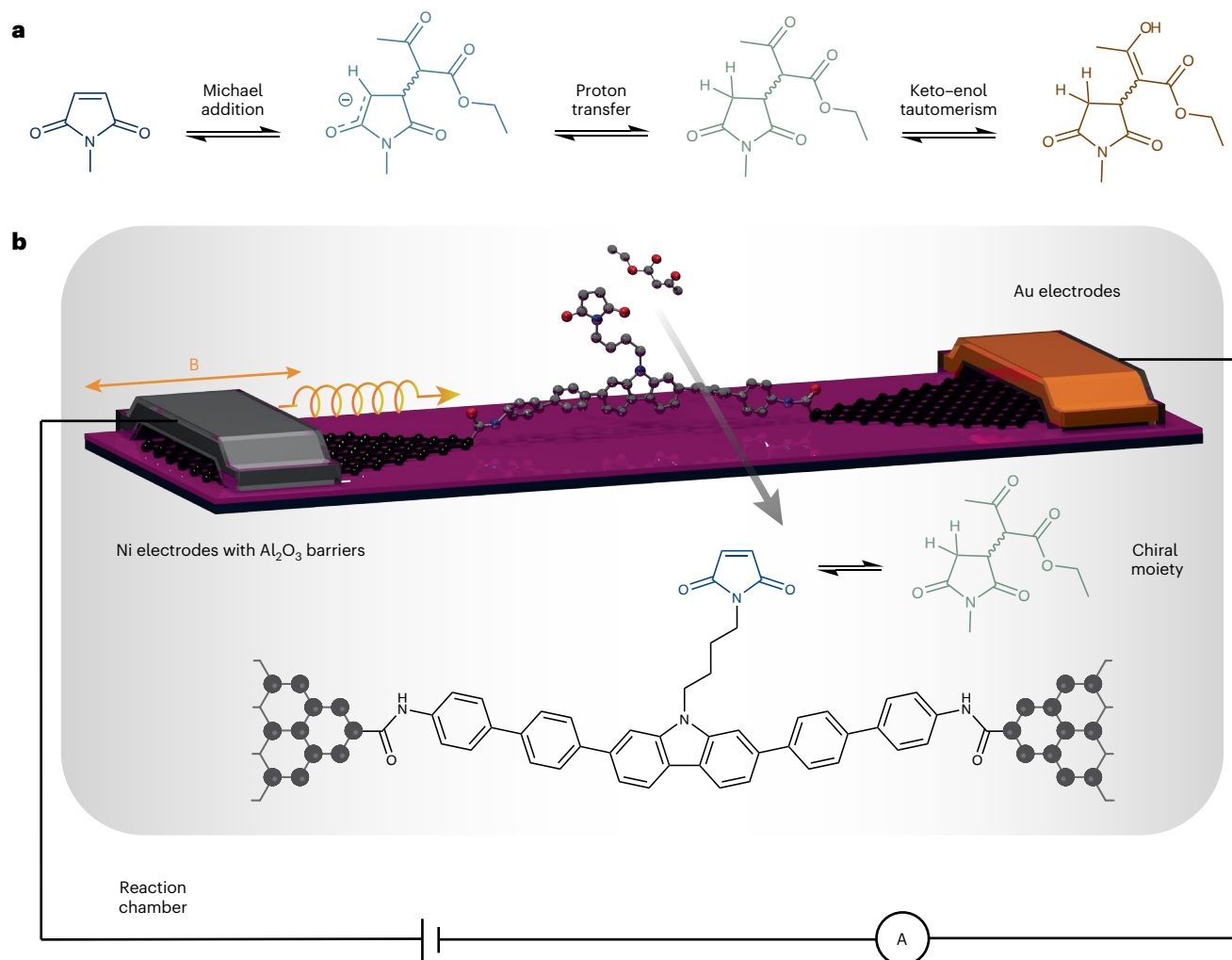


Fig. 1 | Monitoring of the Michael reaction in a molecular junction setup.

a, The Michael addition and subsequent proton transfer and keto-enol tautomerism. **b**, Schematic of our single-molecule spin valve device for identification of the chirality in the Michael addition. Cr (8 nm)/Au (60 nm) and

Al_2O_3 (6 Å)/Ni (80 nm) electrodes (with the latter serving as the ferromagnetic electrode) are coupled via graphene flakes to the chiral moiety. The entire junction is placed in the reaction chamber, such that the electric current is measured as the reactions take place.

expected, leading to the general agreement that the origin of the CISS effect is largely unknown^{18,24}. It is thus expected that the real-time monitoring of chirality variations during chemical reactions via the CISS effect could not only improve our understanding of how chiral symmetry breaking takes place but also shed light on the physical origin of the CISS effect.

One feasible route to achieving this goal is to use single-molecule junctions (that is, single molecules trapped between two electrodes)²⁵. Such single-molecule electrical measurements have enabled the detection of various effects (such as Coulomb blockade²⁶, quantum interference²⁷, superconductivity²⁸, spin selectivity²⁹ and other physical properties^{25,30}), the detection of chemical/biological species³¹ and other device functionalization²⁵. The deciphering of reaction pathways (not only the species)^{32,33} and electron-³⁴ or electric field-induced³⁵ catalysis mechanisms shows the ability of single-molecule transport measurements to reliably elucidate the dynamics at the single-molecule level, beyond the ensemble average³¹. In this Article, we push forward these abilities (including direct observation of addition mechanisms via reaction trajectories, and precise regulation of the energy profile by an electric field) and then demonstrate in situ detection of the formation of a chiral molecular moiety through a symmetry-breaking reaction.

Results and discussion

Electrical monitoring of the Michael addition

A classic example of a chiral symmetry-breaking reaction is the Michael addition of 1,3-dicarbonyl compounds to maleimide^{36,37}. The attack of a base-activated carbanion generates a chiral centre in the maleimide and is followed by hydrogen transfer and keto-enol tautomerization—two important processes in organic synthesis and biology (Fig. 1a). Deciphering this mechanism, clarifying the rate-determining step (RDS) and identifying and resolving chirality are essential steps to optimizing the reaction yield and efficiency. To monitor such a reaction in situ, we developed a hybrid single-molecule junction setup that includes metal-graphene-molecule molecular nanocircuits with a particular magnetized ferromagnetic electrode (see schematic in Fig. 1b).

We prepared Ni/ Al_2O_3 /graphene/single molecule/graphene/Cr/Au devices (Fig. 1b) by evaporating Ni and Au electrodes onto graphene field-effect transistors. The detailed procedure for the preparation of the graphene field-effect transistor and single-molecule device is provided in Supplementary Figs. 1–3. Successful spin injection and transport (up to temperatures of 200 K) from the Ni electrode to graphene was verified using magnetoresistance measurements between two Ni electrodes in a graphene spin valve (see Supplementary Figs. 4–6). The response of drain currents (I_d) versus source-drain

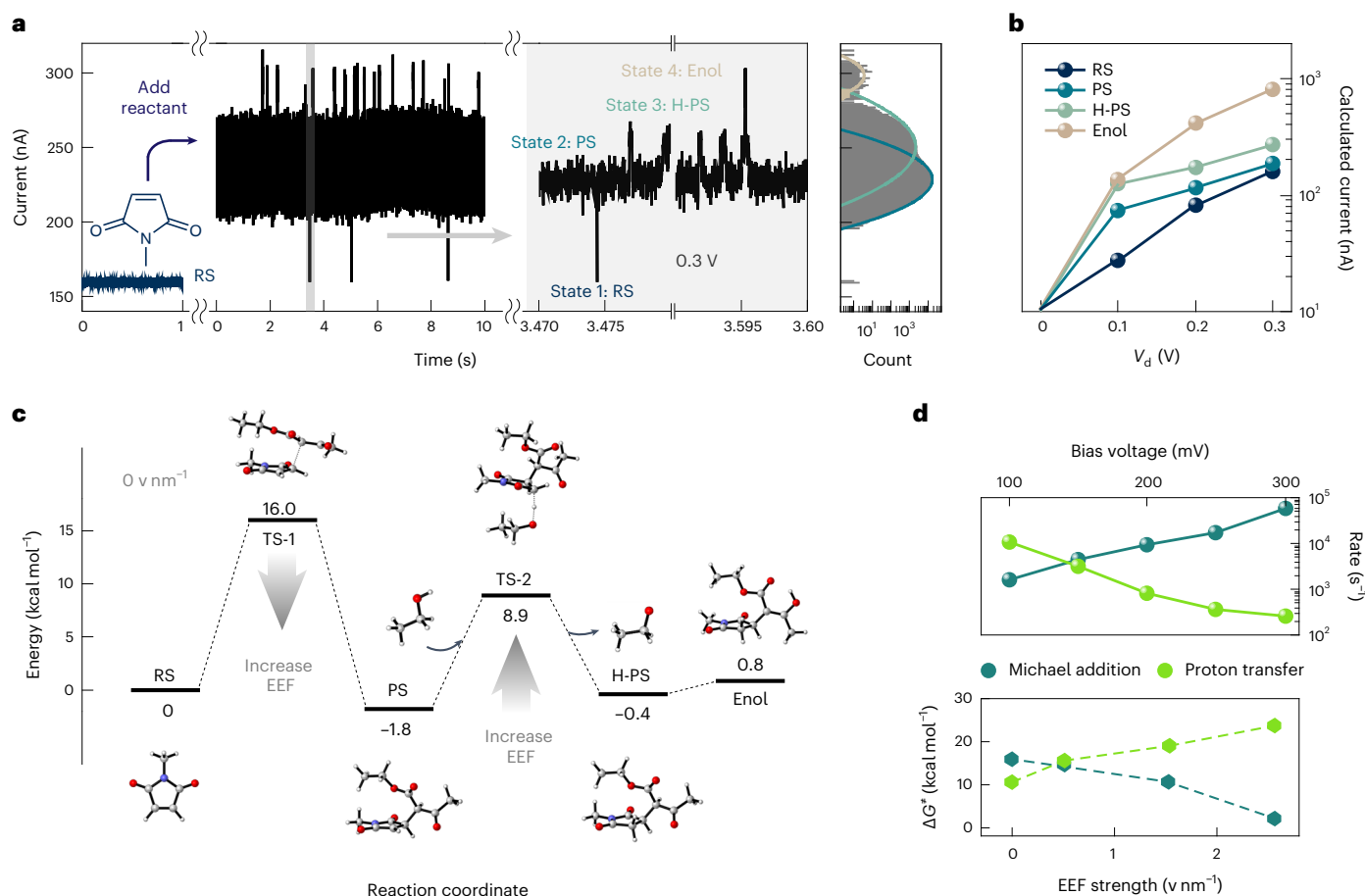


Fig. 2 | Complete description of the Michael addition on a routine Au/Cr/graphene/single molecule/graphene/Cr/Au device. a, Main left, $I-t$ curve of maleimide at 0.3 V, before the reaction took place. Main middle, recorded $I-t$ curve at 0.3 V after adding ethyl acetoacetate and base solution, showing current fluctuations corresponding to different reaction states. Main right, magnification of the shaded area of the middle curve (at ~ 3.5 s). Far right, current histogram of

the 10 s measurements. **b**, Calculated $I-V$ curves of the four assigned species, showing a good match with the observed current histogram. **c**, Potential energy surface of the Michael addition and subsequent processes at 0 v nm^{-1} . **d**, Top, reaction rates versus bias voltage, extracted from the transport data. Bottom, regulation of the reaction by the applied external electric field (EEF)—theoretical calculation. PS, product state; RS, reactant state; TS, transition state.

voltage (V_d) ($I-V$ curves) demonstrates the successful connection of the molecular bridge (Supplementary Fig. 7). Under optimal conditions, the connection yield reached approximately 22%: 16 out of the 72 devices on the same silicon chip showed the $I-V$ response. The difference in currents among single-molecule junctions originates from the different couplings between electrodes and molecules at the atomic scale. Statistical analysis in the Supplementary Information (section ‘Single-molecule connection analysis’) shows that the current response has a probability of resulting from only one molecular connection between the Ni and Au electrodes of around 90%. The connection of the target maleimide-functional molecular bridge can be characterized by the inelastic electron tunnelling spectrum (IETS) (Supplementary Fig. 8a). Both stochastic optical reconstruction microscopy and a high-resolution photoelectrical integration system previously provided direct characterization of the one-maleimide connection³⁸.

For complete transport-based monitoring of the reaction, we conducted current measurements over time ($I-t$ measurements) at a constant bias voltage (set at 0.3 V). To define a reference, we started by measuring the current through a single maleimide (the reactant state (state 1), supported by the IETS in Supplementary Fig. 8a), which was found to be -158 nA . After addition of the reactant (ethyl acetoacetate; $1 \mu\text{M}$) and base (ethanol sodium ethoxide; $1 \mu\text{M}$) in ethanol, four distinct current levels were observed, which can be seen in Fig. 2a (most notably in the right panel, which is a close-up view of the shaded area in the

centre panel). The reactant state can be identified by comparing the $I-t$ curve with that of the bare maleimide. The control experiment of the system without ethyl acetoacetate showed only one current level with $1/f$ noise (Supplementary Fig. 9), which supports that the discrete current changes (regarded as random telegraph signals) originate from chemical reaction (Supplementary Fig. 10). The three other states of the reaction resolved by the $I-t$ plots can be identified as follows. State 2 is attributed to the product state of the Michael addition (implied by the time sequence relationship and the variation of the ratio between states 1 and 2 in reactant concentration-dependent measurements; see Supplementary Fig. 11). State 3 corresponds to the charge-neutral product state (H-PS) of the Michael addition, which can be inferred by the fact that it always follows state 2, further corroborated by the fact that replacing the reactant and base solution with pure ethanol showed a stable state 3. More evidence for this assignment of state 3 results from the IETS analysis (Supplementary Fig. 8b). Finally, state 4 is the state at the highest current level, higher amounts of which are seen in a lower-polarity solvent (see Supplementary Figs. 12 and 13). Solvent-dependent measurements indicate that state 4 is the enol form of H-PS (state 3 is the keto form), showing the reversible keto–enol tautomerism.

In Fig. 2a (right), we plot the current distributions of the four reaction states described above (note that the contribution of state 1 is very low). Figure 2b provides the calculated $I-V$ curves for the four species.

The maxima of the distributions agree well with the theoretical calculations of the currents through states 1–4 (Fig. 2b and Supplementary Figs. 14–16), further corroborating the assignment of the different I - t signals to the different steps of the reaction. This clearly demonstrates the capability of our setup to monitor the reaction paths in detail and in real time.

Using a quantitative analysis of the reaction trajectories (time sequences; Supplementary Figs. 17–19), we derived the kinetic and thermodynamic parameters of the above process and found the proton transfer step to be the RDS. Furthermore, the RDS can be changed by increasing the voltage bias (independent of bias direction), thus allowing the manipulation of chemical reactions in the single-molecule device (Supplementary Figs. 20 and 21 and Fig. 2c,d). The experiment-derived reaction rates at different biases are in good agreement with the energy barriers calculated at different external electric fields (Fig. 2d). The RDS shifts from the proton transfer to the Michael addition with an increase in the bias voltage (Fig. 2c and Supplementary Figs. 22–24), while the signal corresponding to the faster process vanishes due to the temporal resolution of the instrument (~ 17 μ s). Regulation of the reaction potential energy surface via the bias voltage will have an important role in further detection of the stereochemistry in this reaction (see below).

Detection of molecular chirality using the CISS effect

The single-molecule electrical monitoring platform allows a complete description of the Michael addition accompanied by proton transfer and tautomerism. However, the emergence of chirality by the Michael addition cannot be detected via the measurements described above. To detect the chirality, we use the CISS effect, on the basis that different enantiomers display different I - V curves when the Ni electrode is magnetized.

Chiral single-molecule products (H-PSs) with fixed configuration (S) were prepared by reaction between maleimide and ethyl acetoacetate catalysed by chiral 2-aminobenzimidazole (Fig. 3a) in trifluoroacetic acid³⁹. I - V curves were measured at a temperature range from 2–150 K with a bare (unmagnetized) Ni electrode (Fig. 3b). The Ni electrode was then magnetized by applying a $\pm T$ magnetic field parallel (and anti-parallel) to its axis, and the corresponding I - V curves of the stable H-PS species were measured down to 2 K (Fig. 3c–g, dotted lines; data shown for negative biases; see Supplementary Information section ‘CISS effect of the R and S configurations’). In comparison with those of the unmagnetized Ni electrode, these I - V curves show a distinct signature of the CISS effect at low temperatures. At a +2 T (–2 T) magnetization, the currents were lower (higher) than in the absence of a magnetic field, pointing to the promotion (inhibition) of current of majority (minority) spins. This difference was not observed when an achiral maleimide was analysed under the same conditions (Supplementary Fig. 25), and performing the same experiment with the R enantiomer resulted in a permutation of the roles of the majority and minority spins (Supplementary Figs. 26–31), thus providing direct evidence that this spin filtering is indeed due to the CISS effect. In addition, the Michael addition product (which bears only one chiral centre) from the reaction between maleimide and acetylacetone also shows the spin-selective effect, indicating that CISS mainly results from the chiral carbon of the maleimide moiety (Supplementary Figs. 32 and 33).

In monitoring the differences in the I - V curves under Ni magnetization, we observed that these differences (characterized by the so-called CISS polarization $P(V) = \frac{I_+(V) - I_-(V)}{I_+(V) + I_-(V)}$) decrease with an increase in

temperature, finally vanishing at 150 K (Fig. 3h). To explain these findings, we point to the recently proposed spinterface mechanism for the CISS effect^{20,23}, in which the CISS effect is attributed to the spin–torque interaction between the (spin–orbit-induced) surface magnetization in the metallic (Au) electrode and the spin imbalance in the chiral molecule, prompted by the chirality-induced (solenoid) field in the molecule (see the Supplementary Information section ‘Theoretical calculation of the CISS effect’ for a full description). Although the chiral moiety is non-helical and not within the main conduction path of the molecular junction, it does break the symmetry and therefore allows for the CISS effect. To fit the simulation model to the data, we started by fitting the bare current (with no magnetization) with a simple model for current through a molecular junction (namely, a Landauer formula, $J(V) = \frac{2e}{h} \int T(E)(f_L(E) - f_R(E))$ with a Lorentzian transmission function $T(E) = \frac{\Gamma^2}{\Gamma^2 + (E - \varepsilon_0)^2}$), where $f_{L,R}$ are the Fermi distributions for the left and right electrodes, Γ and ε_0 are the molecular level broadening and frontier orbital energy, and e and h are the electron charge and Planck constant, respectively. These fits (Fig. 3b, solid lines) provide us with the molecular parameter $\varepsilon_0 = -0.34$ eV and a phenomenological level broadening $\Gamma(T) = 0.0015 + 0.002 T^{0.23}$ eV (with T in degrees K; see the Supplementary Information section ‘Theoretical calculation of the CISS effect’ and Supplementary Fig. 34).

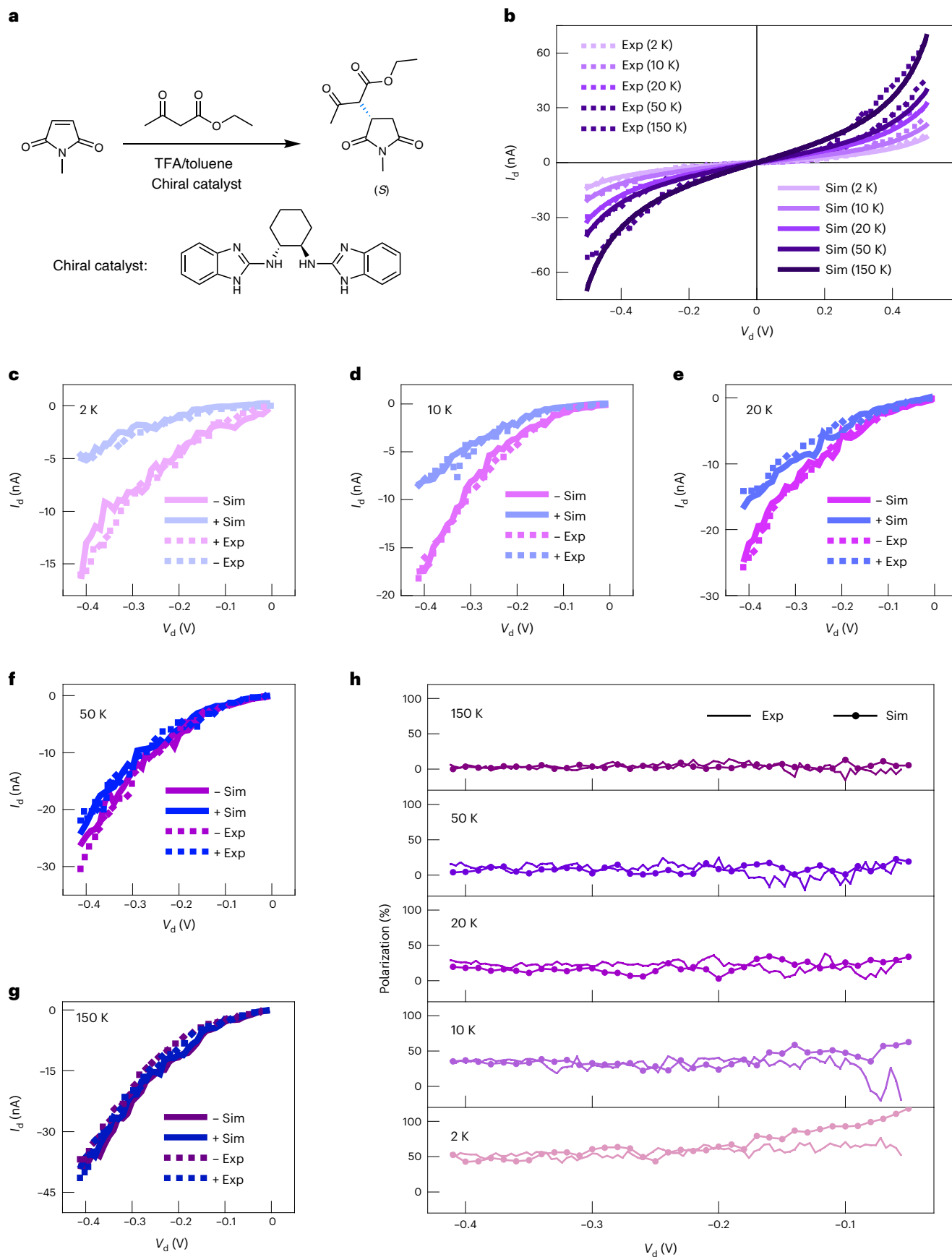
With these molecular parameters, we then fit the spin-dependent curves at 2 K (Fig. 3c, solid lines) using the spinterface theory, where the extracted parameters were the Au spin–orbit coupling α_A and the spin–torque coupling α_1 (see the Supplementary Information section ‘Theoretical calculation of the CISS effect’). The fits yielded $\alpha_A = 0.6$ eV⁴⁰ and $\alpha_1 = 2.2$ meV. Using these parameters, we then simulated the spin-dependent curves at $T = 10, 20, 50$ and 150 K (solid lines in Fig. 3d–g) with no additional fitting (Supplementary Fig. 35). The vanishing CISS effect with an increase in temperature is attributed to both temperature-induced fluctuations of the surface magnetization and broadening of the Fermi distributions²⁰. Finally, the polarizations $P(V)$ at different temperatures showed a close fit between the data and theory (dashed and solid lines in Fig. 3h). The excellent agreement between the data and simulations (with no CISS-related fitting parameters being necessary for the $T > 2$ K data) strongly supports the validity of our model and corroborates the spinterface mechanism for the CISS effect. Note that the vanishing of the CISS effect with an increase in temperature is consistent with previous literature¹⁶. However, it is rather atypical for the CISS effect to vanish completely well below room temperature^{41–43}. We attribute this result to the weakly coupled nature of the molecular junction (as reflected by the small level broadening Γ , which is smaller than $k_B T$ at room temperature) and to the small value of the spin–torque coupling α_1 (which may arise due to the effective distance between the metal electrode and the molecular bridge, separated by the graphene electrode).

Real-time monitoring of molecular chirality

The measurement platform described here allows us to go beyond the usual measurements of the CISS effect and to monitor—in situ and in real time—the changes in the chirality of the molecular moiety. Such monitoring can be achieved by cooling down the reaction system in the absence of a chiral catalyst (Fig. 4a). For a fixed Ni magnetization, flipping the molecular chirality reverses the roles of the majority and minority spin carriers and leads to an abrupt change in current.

Fig. 3 | Single-molecule spin filtering and the CISS effect. **a**, Strategy for preparing a fixed-configuration product of the Michael addition. TFA, trifluoroacetic acid. **b**, Experimental (exp) and simulated (sim) I - V curves of the single-molecule spin valve under different temperatures at 0 T. **c–g**, Experimental and simulated I - V curves of the single-molecule spin valve at 2 K (**c**), 10 K (**d**), 20 K (**e**), 50 K (**f**) or 150 K (**g**) in a magnetic field of –2 T (marked with a minus

sign) or +2 T (marked with a plus sign). The clear differences between the curves at +2 T and –2 T are the hallmark of the CISS effect. Theoretical simulations showed good agreement between data and theory; no additional fit parameters were used for **d–g**. **h**, Experimental and simulated polarization versus bias voltage at various temperatures.



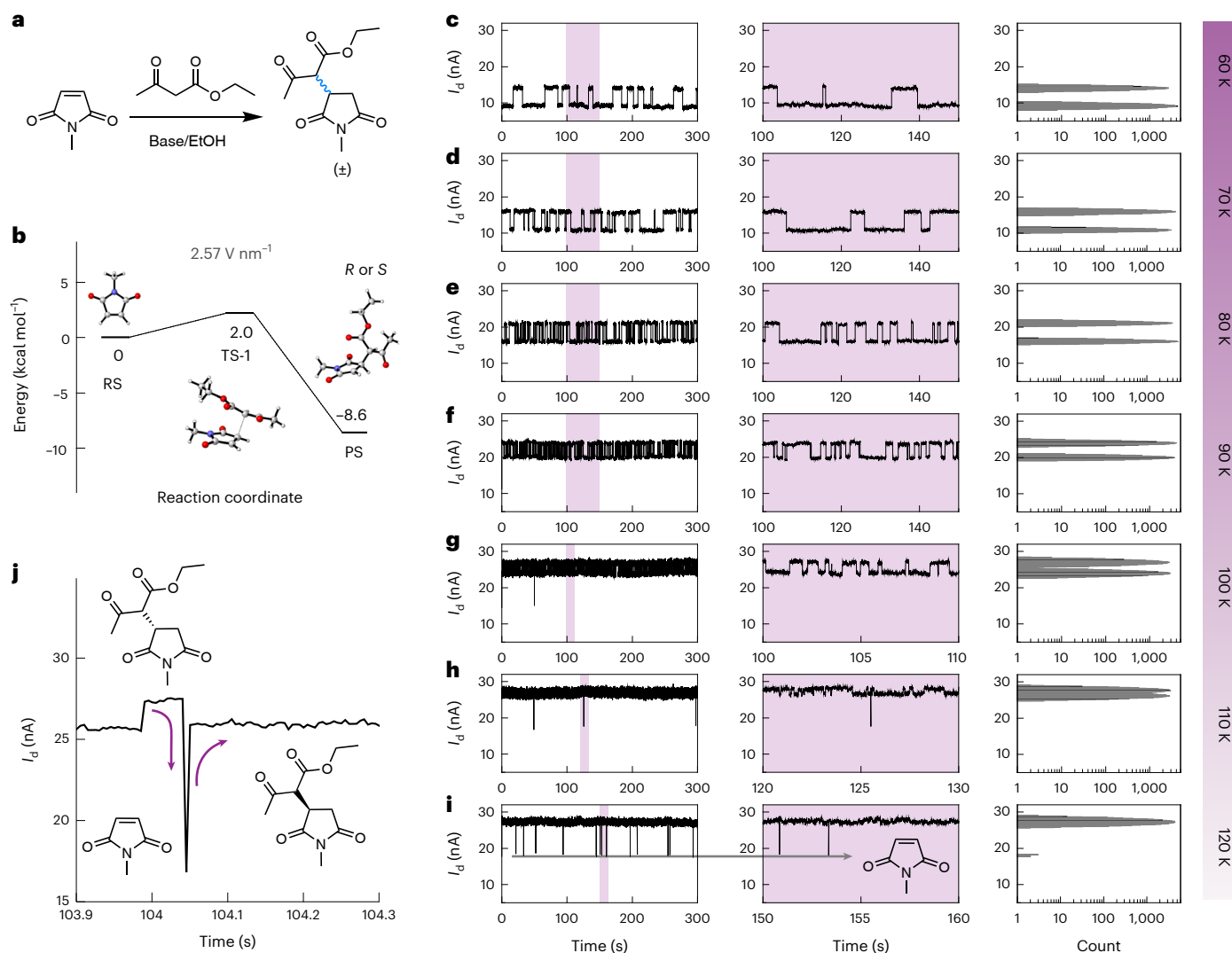


Fig. 4 | Real-time monitoring of chirality variations during the reaction.

a, Schematic of the chiral Michael addition reaction measured at the molecular junction. **b**, Potential energy surface of the Michael addition at 2.57 V nm^{-1} . **c–i**, Real-time monitoring of the current during the chiral Michael addition at

temperatures of 60 K (**c**), 70 K (**d**), 80 K (**e**), 90 K (**f**), 100 K (**g**), 110 K (**h**) and 120 K (**i**). **j**, A typical time sequence of the electrical signal at 110 K and at high temporal resolution. The maleimide is an inevitable intermediate between the *R* and *S* configurations.

The real-time monitoring of chirality is compromised by temperature in two ways: (1) by the vanishing of the CISS effect at $\sim 120 \text{ K}$; and (2) by the reduction of the reaction activity at low temperatures (at least at low bias voltages; see Supplementary Fig. 20). However, the reaction can be pushed to lower temperatures by applying a strong bias voltage. Benefiting from the ensuing external electric fields at high voltages, the transition state of the Michael addition can be reduced ($\Delta G^{\ddagger}_{\text{Michael addition}} \sim 2.2 \text{ kcal mol}^{-1}$ and $\Delta G^{\ddagger}_{\text{retro Michael addition}} \sim 10.6 \text{ kcal mol}^{-1}$ at 2.57 V nm^{-1} ; Fig. 4b and Supplementary Fig. 24). The use of a relatively large bias voltage allowed us to lower the temperature to $\sim 60 \text{ K}$ and still observe the reaction.

We then recorded I - t curves of the reaction system at 60–120 K with a +2 T magnetization of the Ni electrode and a 0.3 V bias voltage (Fig. 4c–i). The centre column of Fig. 4c–i is a magnification of the shaded area shown in the left column, whereas the right column of Fig. 4c–i shows a histogram of the current levels. At 60 K, the measurement clearly shows the two enantiomers, thus proving our ability to detect the chirality flipping. We corroborated this by showing that the two signals could be recorded at a flipped Ni magnetization in the same device (-2 T ; marked as device 1 in Supplementary Fig. 36), whereas no asymmetry was found in the absence of Ni magnetization

(0 T; Supplementary Fig. 37). These phenomena could be reproducibly observed on other devices (devices 2–4 in Supplementary Figs. 38–46).

Direct conversion between the *R* and *S* configurations of the studied product (chiral inversion at one carbon atom) is essentially impossible due to steric hindrance. Instead, *R*-*S* conversion must go through the achiral maleimide intermediate, which by itself is unstable and short lived at 60 K (as seen in Fig. 4j) on a fast time resolution but not in Fig. 4c because of temporal resolution). This implies that each of the conversions between *R* and *S* represents a pair of reverse and forward reaction trajectories. The actual number of reaction trajectories might be higher than the number of *R/S* binary switching events because the same configuration may be obtained among adjacent reverse/forward reaction event pairs.

The temperature-dependent I - t measurement sheds further light on the Michael addition. As the temperature increases, faster *R/S* switching indicates a higher reaction rate (Fig. 4c–i), which is in line with the Arrhenius equation. Meanwhile, the maleimide state (Fig. 4h–j; low-current spikes) appears gradually (Fig. 4g–i), implying a shift in the equilibrium. This can be illustrated clearly at a lower bias voltage (0.05 V, where the Michael addition is the dominating process) from 278–318 K because of the statistical significance (Supplementary

Fig. 47). The Arrhenius (Supplementary Fig. 48) and Van't Hoff plots (Supplementary Fig. 49) are indicative of an exothermic Michael addition, which supports the occupancy variations of the maleimide at 60–120 K.

Conclusions

As demonstrated above, the real-time monitoring of currents in single-molecule junctions allows us to follow the individual steps of complex (multi-step) chiral symmetry-breaking reactions and to determine the resulting chirality of the chemical product. This was exemplified with a Michael addition (one of the classical reactions in organic synthesis³⁶) in which the different steps of the reaction were characterized by a specific current–voltage response, which could be detected electrically.

To detect the chiral products, we used a spin valve setting of the molecular junction. This setting, applied at different temperatures (in a range of 2–150 K), allowed us to quantify the response of the different enantiomers to an applied voltage via the CISS effect. The data successfully fit a model based on the spinterface theory for the CISS effect²⁰, shedding new light on the (highly debated) origin of the CISS effect. Finally, we demonstrated that the CISS effect could be used to track chirality changes in situ at the molecular junction.

Future studies will be aimed at using the spin current generated by the CISS effect to drive asymmetric catalysis directly, thus avoiding the need to carefully design suitable asymmetric catalysts. The ability to covalently fix the molecular chiral reaction centre in molecular nanodevices will become key to linking the spin orientation and the molecular frame, so as to achieve direct asymmetric catalysis by spin currents. Our setup will also allow us to deepen our understanding of the CISS effect by performing additional experiments aimed at discriminating between the different theories on its origin, for instance replacing the Au electrodes with other metals and using chiral molecular moieties with a repeating unit, among others²⁰. Finally, in situ synchronous characterizations of single molecules in combination with other spectroscopies (such as Raman spectroscopy⁴⁴ and photoemission electron spectroscopy⁴⁵, which provide more definitive structure-related information) are worth pursuing, as these will increase the ability to relate current variations to chemical and structural variations, thus allowing us to decipher and regulate more complex reactions.

Online content

Any methods, additional references, Nature Portfolio reporting summaries, source data, extended data, supplementary information, acknowledgements, peer review information; details of author contributions and competing interests; and statements of data and code availability are available at <https://doi.org/10.1038/s41557-023-01212-2>.

References

- Dalko, P. I. & Moisan, L. In the golden age of organocatalysis. *Angew. Chem. Int. Ed.* **43**, 5138–5175 (2004).
- Bornscheuer, U. T. et al. Engineering the third wave of biocatalysis. *Nature* **485**, 185–194 (2012).
- Hsieh, D. et al. Observation of unconventional quantum spin textures in topological insulators. *Science* **323**, 919–922 (2009).
- Hendry, E. et al. Ultrasensitive detection and characterization of biomolecules using superchiral fields. *Nat. Nanotechnol.* **5**, 783–787 (2010).
- Tu, H.-F., Yang, P., Lin, Z.-H., Zheng, C. & You, S.-L. Time-dependent enantiodivergent synthesis via sequential kinetic resolution. *Nat. Chem.* **12**, 838–844 (2020).
- Yeom, J. et al. Chiro-magnetic nanoparticles and gels. *Science* **359**, 309–314 (2018).
- Tang, Y. & Cohen Adam, E. Enhanced enantioselectivity in excitation of chiral molecules by superchiral light. *Science* **332**, 333–336 (2011).
- Banerjee-Ghosh, K. et al. Separation of enantiomers by their enantiospecific interaction with achiral magnetic substrates. *Science* **360**, 1331–1334 (2018).
- Kumar, J. et al. Detection of amyloid fibrils in Parkinson's disease using plasmonic chirality. *Proc. Natl Acad. Sci. USA* **115**, 3225–3230 (2018).
- Steendam, R. R. E. et al. Emergence of single-molecule chirality from achiral reactants. *Nat. Commun.* **5**, 5543 (2014).
- Gohler, B. et al. Spin selectivity in electron transmission through self-assembled monolayers of double-stranded DNA. *Science* **331**, 894–897 (2011).
- Naaman, R., Paltiel, Y. & Waldeck, D. H. Chiral molecules and the electron spin. *Nat. Rev. Chem.* **3**, 250–260 (2019).
- Kim, Y. H. et al. Chiral-induced spin selectivity enables a room-temperature spin light-emitting diode. *Science* **371**, 1129–1133 (2021).
- Naaman, R., Paltiel, Y. & Waldeck, D. H. Chiral molecules and the spin selectivity effect. *J. Phys. Chem. Lett.* **11**, 3660–3666 (2020).
- Aragones, A. C. et al. Measuring the spin-polarization power of a single chiral molecule. *Small* **13**, 1602519 (2017).
- Naaman, R. & Waldeck, D. H. Spintronics and chirality: spin selectivity in electron transport through chiral molecules. *Annu. Rev. Phys. Chem.* **66**, 263–281 (2015).
- Al-Bustami, H. et al. Single nanoparticle magnetic spin memristor. *Small* **14**, 1801249 (2018).
- Brandt, J. R., Salerno, F. & Fuchter, M. J. The added value of small-molecule chirality in technological applications. *Nat. Rev. Chem.* **1**, 0045 (2017).
- Michaeli, K., Kantor-Uriel, N., Naaman, R. & Waldeck, D. H. The electron's spin and molecular chirality—how are they related and how do they affect life processes? *Chem. Soc. Rev.* **45**, 6478–6487 (2016).
- Alwan, S. & Dubi, Y. Spinterface origin for the chirality-induced spin-selectivity effect. *J. Am. Chem. Soc.* **143**, 14235–14241 (2021).
- Ghazaryan, A., Paltiel, Y. & Lemeshko, M. Analytic model of chiral-induced spin selectivity. *J. Phys. Chem. C* **124**, 11716–11721 (2020).
- Qi, D., Kenaan, A., Cui, D. & Song, J. Novel insights into the selection to electron's spin of chiral structure. *Nano Energy* **52**, 142–152 (2018).
- Dubi, Y. Spinterface chirality-induced spin selectivity effect in bio-molecules. *Chem. Sci.* **13**, 10878–10883 (2022).
- Evers, F., Korytár, R., Tewari, S. & van Ruitenbeek, J. M. Advances and challenges in single-molecule electron transport. *Rev. Mod. Phys.* **92**, 035001 (2020).
- Xin, N. et al. Concepts in the design and engineering of single-molecule electronic devices. *Nat. Rev. Phys.* **1**, 211–230 (2019).
- Park, J. et al. Coulomb blockade and the Kondo effect in single-atom transistors. *Nature* **417**, 722–725 (2002).
- Bai, J. et al. Anti-resonance features of destructive quantum interference in single-molecule thiophene junctions achieved by electrochemical gating. *Nat. Mater.* **18**, 364–369 (2019).
- Winkelmann, C. B., Roch, N., Wernsdorfer, W., Bouchiat, V. & Balestro, F. Superconductivity in a single-C₆₀ transistor. *Nat. Phys.* **5**, 876–879 (2009).
- Kim, W. Y. & Kim, K. S. Tuning molecular orbitals in molecular electronics and spintronics. *Acc. Chem. Res.* **43**, 111–120 (2010).
- Waldrop, M. M. The chips are down for Moore's law. *Nat. News* **530**, 144–147 (2016).
- Li, Y., Yang, C. & Guo, X. Single-molecule electrical detection: a promising route toward the fundamental limits of chemistry and life science. *Acc. Chem. Res.* **53**, 159–169 (2020).
- Yang, C. et al. Single-molecule electrical spectroscopy of organocatalysis. *Matter* **4**, 2874–2885 (2021).

33. Yang, C. et al. Unveiling the full reaction path of the Suzuki–Miyaura cross-coupling in a single-molecule junction. *Nat. Nanotechnol.* **16**, 1214–1223 (2021).
34. Chen, H. et al. Electron-catalyzed dehydrogenation in a single-molecule junction. *J. Am. Chem. Soc.* **143**, 8476–8487 (2021).
35. Aragones, A. C. et al. Electrostatic catalysis of a Diels–Alder reaction. *Nature* **531**, 88–91 (2016).
36. Huang, G. & Li, X. Applications of Michael addition reaction in organic synthesis. *Curr. Org. Synth.* **14**, 568–571 (2017).
37. Sibi, P. M. & Manyem, S. Enantioselective conjugate additions. *Tetrahedron* **56**, 8033–8061 (2000).
38. Yang, C. et al. Electric field–catalyzed single-molecule Diels–Alder reaction dynamics. *Sci. Adv.* **7**, eabf0689 (2021).
39. Gómez-Torres, E., Alonso, D. A., Gómez-Bengoña, E. & Nájera, C. Enantioselective synthesis of succinimides by Michael addition of 1,3-dicarbonyl compounds to maleimides catalyzed by a chiral bis(2-aminobenzimidazole) organocatalyst. *Eur. J. Org. Chem.* **2013**, 1434–1440 (2013).
40. Gersten, J., Kaasbjerg, K. & Nitzan, A. Induced spin filtering in electron transmission through chiral molecular layers adsorbed on metals with strong spin–orbit coupling. *J. Chem. Phys.* **139**, 114111 (2013).
41. Xie, Z. et al. Spin specific electron conduction through DNA oligomers. *Nano Lett.* **11**, 4652–4655 (2011).
42. Kondou, K. et al. Chirality-induced magnetoresistance due to thermally driven spin polarization. *J. Am. Chem. Soc.* **144**, 7302–7307 (2022).
43. Das, T. K., Tassinari, F., Naaman, R. & Fransson, J. Temperature-dependent chiral-induced spin selectivity effect: experiments and theory. *J. Phys. Chem. C* **126**, 3257–3264 (2022).
44. Jeong, H., Li, H. B., Domulevicz, L. & Hihath, J. An on-chip break junction system for combined single-molecule conductance and Raman spectroscopies. *Adv. Funct. Mater.* **30**, 2000615 (2020).
45. Badala Viswanatha, C. et al. Vectorial electron spin filtering by an all-chiral metal–molecule heterostructure. *J. Phys. Chem. Lett.* **13**, 6244–6249 (2022).

Publisher's note Springer Nature remains neutral with regard to jurisdictional claims in published maps and institutional affiliations.

Springer Nature or its licensor (e.g. a society or other partner) holds exclusive rights to this article under a publishing agreement with the author(s) or other rightsholder(s); author self-archiving of the accepted manuscript version of this article is solely governed by the terms of such publishing agreement and applicable law.

© The Author(s), under exclusive licence to Springer Nature Limited 2023, corrected publication 2024

Methods

Device fabrication and molecular connection

High-quality single-layer graphene was grown on a 25- μm -thick copper sheet by high-temperature chemical vapour deposition. This graphene was then transferred to a 1.5 cm \times 1.5 cm silicon wafer with a 300 nm SiO₂ layer after etching the copper. Then, the graphene was protected by a mask and etched by oxygen plasma to obtain a 20- μm -wide graphene sheet. The array of drain electrodes (0.6 nm Al (post-oxidation to Al₂O₃), 80 nm Ni and 40 nm SiO₂) was evaporated successively using the template method. Similarly, the array of source electrodes (8 nm Cr, 60 nm Au and 40 nm SiO₂) was evaporated successively using the template method. To prepare the array of graphene nanosized gaps between pairs of source and drain metal electrodes, a dashed-line pattern was designed with 150 nm length and 5 nm width and prepared on pre-spin-coated polymethylmethacrylate (PMMA) by electron beam lithography, where the beam current was -0.17 nA and the area dose was -2,600 $\mu\text{C cm}^{-2}$. Graphene exposed from the dashed-line window was then etched by oxygen plasma. By exploiting the gradual etching of PMMA and isotropous broadening, we achieved a series of narrow gaps (-1–10 nm) with carboxyl terminals between indented graphene point contacts (~210 pairs). Complete cutting of graphene electrodes was characterized by an open circuit between the corresponding metal electrode pairs (this was not present before cutting). The incompletely etched graphene was checked by I - V scanning and then electrically burned (from 0–10 V) to ensure that the subsequent current recovery originated from molecular junctions.

To integrate one molecule into the electrode pairs, freshly prepared graphene devices with a point electrode array were added to a pyridine solution containing 0.1 mM of the molecular bridge (deprotection of Boc by CF₃COOH) and 1 mM 1-(3-dimethylaminopropyl)-3-ethylcarbodiimide hydrochloride³⁸. After 48 h, the devices were removed from the solution and rinsed with deionized water, followed by drying with flowing N₂. Finally, the molecular bridge (which fit the nanogap) was integrated into graphene electrodes via amide bonds.

Electrical characterization

The single-molecule device was placed in a vacuum cryogenic probe station (Lake Shore TTPX for routine measurements) or Physical Property Measurement System to perform the chirality measurements. The I - V curves were measured using an Agilent 4155C semiconductor parameter system. The auxiliary output of a UHFLI lock-in amplifier gave a constant bias for the I - t measurement. The current signal of the molecular loop was amplified using a DL1211 amplifier and then recorded with a high-speed acquisition card from NI DAQ at a rate of 57,600 samples per second.

Data availability

Additional discussions and data supporting this article are available in the Supplementary Information. Source data are provided with this paper.

Acknowledgements

We acknowledge primary financial support from the National Key R&D Program of China (2022YFE0128700, 2017YFA0204901 and 2021YFA1200101), National Natural Science Foundation of China (22150013, 22173050, 21727806 and 21933001), Tencent Foundation (through the Xplorer Prize), Natural Science Foundation of Beijing (2222009) and Frontiers Science Center for New Organic Matter at Nankai University (63181206). Y.D. acknowledges support from the Israel Science Foundation (1360/17). S.Z. and Z.L. appreciate support from the High-Performance Computing Platform of the Center for Life Science (Peking University) and High-Performance Computing Platform of Peking University.

Author contributions

X.G., Y.D. and K.N.H. conceived of and designed the experiments. C.Y., Y.G. and C.J. fabricated the devices and performed the device measurements. Y.D., Y.L., S.Z. and Z.L. built and analysed the theoretical model and performed the quantum transport calculation. X.G., Y.D., K.N.H. and C.Y. analysed the data and wrote the paper. All authors discussed the results and commented on the manuscript.

Competing interests

The authors declare no competing interests.

Additional information

Supplementary information The online version contains supplementary material available at <https://doi.org/10.1038/s41557-023-01212-2>.

Correspondence and requests for materials should be addressed to Kendall N. Houk, Yonatan Dubi or Xuefeng Guo.

Peer review information *Nature Chemistry* thanks Ismael Diez Perez, Kun Wang and the other, anonymous, reviewer(s) for their contribution to the peer review of this work.

Reprints and permissions information is available at www.nature.com/reprints.